Available online at www.sciencedirect.com
ScienceDirect
European Journal of Mechanics B/Fluids 27 (2008) 388–408

Turbulence manipulation in air–water flows on a stepped chute: An experimental study

C.A. Gonzalez [a], H. Chanson [b,*]

[a] *Water Engineer, Cardno Pty Ltd, Level 1, 5 Gardner Close, Milton, QLD 4064, Australia* [1]
[b] *Professor in Civil Engineering, Div. of Civil Engineering, The University of Queensland, Brisbane QLD 4072, Australia*

Received 24 April 2007; received in revised form 31 July 2007; accepted 26 September 2007

Available online 3 October 2007

Abstract

In a stepped channel operating with large flow rates, the flow skims over the pseudo-bottom formed by the step edges as a coherent stream. Intense three-dimensional recirculation is maintained by shear stress transmission from the mainstream to the step cavities, while significant free-surface aeration takes place. The interactions between free-surface aeration and cavity recirculation are investigated herein with seven step cavity configurations. The experiments were conducted in a large stepped channel operating at large Reynolds numbers. For some experiments, triangular vanes, or longitudinal ribs, were placed across the step cavities to manipulate the flow turbulence to enhance the interactions between the mainstream flow and the cavity recirculation region. The results showed a strong influence of the vanes on the air–water flow properties in both free-stream and cavity flows. The findings demonstrate some passive turbulence manipulation in highly turbulent air–water flows.

Keywords: Skimming flows; Cavity recirculation; Turbulence manipulation; Momentum transfer; Air bubble entrainment

1. Introduction

Several researchers studied the air bubble entrainment in liquid flows, typically in fluids with low void fractions ($C < 5\%$) and relatively low Reynolds numbers [1,2]. Very few studies considered strong free-surface aeration in highly-turbulent flows [3–5]. One such flow is the supercritical open channel flow skimming down a stepped channel. Skimming flows are highly-turbulent self aerated flows commonly observed on overflow spillways of gravity and embankment dams [6]. There is some analogy between skimming flows over a stepped chute and skimming flows above large roughness elements, including boundary layer flows past d-type roughness. Djenidi et al. [7] provided a comprehensive review of the latter, while Aivazian [8] studied the flow over roughness elements placed in zigzag. Mochizuki et al. [9,10] studied turbulent boundary layer development past d-type roughness equipped with thin longitudinal ribs.

* Corresponding author.
E-mail address: h.chanson@uq.edu.au (H. Chanson).
URL: http://www.uq.edu.au/~e2hchans (H. Chanson).
[1] Formerly: Div. of Civil Engineering, The University of Queensland, Australia.

0997-7546/$ – see front matter
doi:10.1016/j.euromechflu.2007.09.003

Despite conflicting interpretations of their data, their experiments demonstrated that turbulence manipulation can be achieved by interfering with the recirculation vortices.

In civil engineering, modern stepped spillways are designed with flat horizontal steps, but some are equipped with devices to enhance the rate of energy dissipation. Some channels incorporate pooled steps with vertical walls, inclined upward steps, rounded edges or alternate sills (Fig. 1). Energy dissipation in stepped chutes can be enhanced by superposing small and large steps, incorporating occasional large drops among small steps, or by using V-shaped step edges [11]. All these techniques may effectively dissipate the flow energy, but their attractiveness is counterbalanced by the needs of extraordinary placement methods for structural integrity.

In the present study, a stepped channel was equipped with different configurations of triangular vanes, or longitudinal ribs, acting as passive turbulence manipulators. The vanes were selected because their load on the structure of the chute is minimal. The purpose of the vanes was to enhance the interactions between mainstream and cavity recirculation regions by altering their three-dimensional nature of the air–water flow. Systematic two-phase flow measurements were performed. It is believed that the present study is the first successful application of passive turbulent manipulation of two-phase flows in high-velocity turbulent open channels. Although the ultimate goal of the vanes is to enhance energy dissipation, the aim of this paper is to document the basic physical processes causing turbulent dissipation and air–water mass transfer, and the influence of the vanes on the microscopic structure of the flow.

2. Experimental apparatus

The experimental measurements were conducted in a 3.3 m long, 1 m wide stepped chute located in the Gordon McKay Hydraulics Laboratory at the University of Queensland. The facility consisted of a basin connected to a chute via a convergent wall with a 4.8:1 ratio (Fig. 2). The test section included a broad crested weir (1 m wide, 0.62 m long) followed by ten identical steps ($h = 0.1$ m, $l = 0.25$ m) made of marine ply. The stepped chute was followed by a horizontal stilling basin ending in a recirculation pit. A pump connected to a Toshiba™ (T-vert VF-A5P) electronic inverter ensured a fine control of the flow rate during experiments. The present experiments were performed at large flow rates corresponding to Reynolds number within $4\,\mathrm{E}+5 < Re < 9\,\mathrm{E}+5$.

Seven step geometries were tested systematically (Table 1). The reference geometry (configuration 1) included ten smooth horizontal steps. For the other geometries (config. 2 to 7), the channel was equipped with vanes (longitudinal thin ribs) placed across the step cavities along the chute width from steps 2 to 10 as illustrated in Fig. 3. The ribs acted as passive turbulent generators which added minimum structural loads to the chute structure. Different arrangements of vanes were tested. The configurations 2 and 3 had three vanes per step placed in line and in zigzag respectively while configurations 4 and 5 had seven vanes set in the same fashion. Configurations 6 and 7 had seven vanes set in line and in zigzag respectively, but these were placed every 2 steps (Fig. 3). The triangular vanes were made of 1.6 mm thick aluminium, although a few vanes placed were made of 6 mm thick perspex for flow visualisation next to the sidewall. The vanes did not interfere with the free-stream.

2.1. Instrumentation and signal processing

Clear-water flow depths were measured with a point gauge. The air–water flow properties were recorded with a double-tip conductivity probe ($\varnothing = 0.025$ mm) designed at the University of Queensland. The translation of the probe in the direction perpendicular to the flow direction was conducted with a screw-drive traverse mechanism fitted with a Mitutoyo™ digimatic scale unit.

The probe sensors were excited by an air-bubble detector and the probe output signal was scanned at 20 kHz during 20 seconds per probe tip. (For a more detailed description of the probe and the air-bubble detector, refer to Chanson [12], Cummings [13] and Toombes [14].) The voltage outputs allowed the calculation of the basic air–water flow properties, including void fraction, interfacial velocity, turbulence intensity, bubble count rate, and chord size distributions.

The void fraction C is the amount of time that the probe tip is in the air. The bubble count rate F is the number of bubbles impacting the probe tips per second. The bubble chord size distributions provide information on the air–water flow micro-structure.

(A)

(B)

Fig. 1. Photographs of spillway stepped channels. (A) Le Pont dam spillway (France, 1882) equipped with pooled stepped spillway and circular step crests. (B) Neil Turner stepped weir (Australia, 1984) with alternate sills at step edges (Courtesy of Chris Proctor).

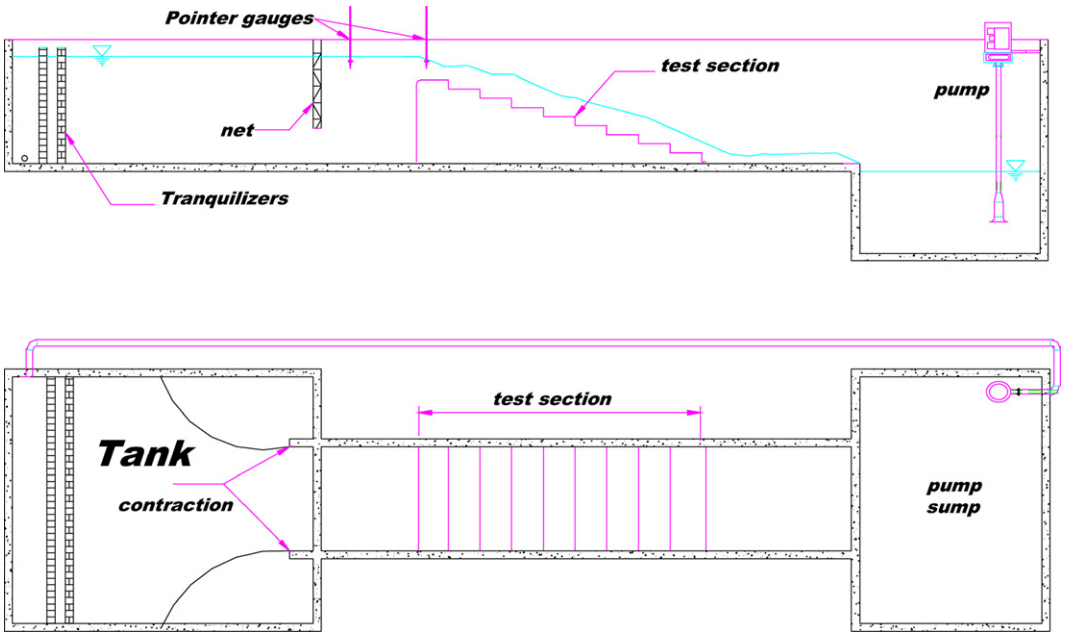

Fig. 2. Sketch of the experimental channel (not drawn to scale).

Table 1
Detailed experimental investigations of air entrainment on stepped channels

Reference (1)	θ deg. (2)	q_w m^2/s (3)	h m (4)	Re (5)	Remarks (7)
Chanson and Toombes [17]	21.8	0.06 to 0.18	0.1	2.4 E + 5 to 7.2 E + 5	$L = 3.0$ m. $W = 1$ m. Inflow: uncontrolled broad-crest. Experiments TC200.
	15.9	0.07 to 0.19	0.1	2.8 E + 5 to 7.6 E + 5	$L = 4.2$ m. $W = 1$ m. Inflow: uncontrolled broad-crest. Experiments TC201.
Gonzalez and Chanson [24]	15.9	0.020 to 0.200	0.05	8 E + 4 to 8 E + 5	$L = 4.2$ m. $W = 1$ m. Inflow: uncontrolled broad-crest. Experiments CG202.
		0.075 to 0.220	0.10	3 E + 5 to 8.7 E + 5	Incl. detailed measurements between step edges.
Present study	21.8	0.10 to 0.22	0.1	4 E + 5 to 8.7 E + 5	$L = 3.3$ m. $W = 1$ m. Inflow: uncontrolled broad-crest. Experiments CG203.
Configuration 1					$b = W = 1$ m (no vane).
Configuration 2					$b = W/4 = 0.250$ m (3 vanes in line every step).
Configuration 3					$b = W/4 = 0.125$ m (3 vanes in zigzag every step).
Configuration 4					$b = W/8 = 0.125$ m (7 vanes in line every step).
Configuration 5					$b = W/8 = 0.125$ m (7 vanes in zigzag every step).
Configuration 6					$b = W/8 = 0.125$ m (7 vanes in line every 2 steps).
Configuration 7					$b = W/8 = 0.125$ m (7 vanes in zigzag every 2 steps).

Notes: L: test section length; W: chute width; h: vertical step height.

The interfacial velocity measurement was based upon the successive detection of air–water interfaces by both probe tips. Although, in turbulent air–water flows, the detection of the same bubbles by both tips is highly improbable, a cross-correlation technique was used to overcome this limitation [15]. The time-averaged velocity was estimated as

$$V = \frac{X}{T} \tag{1}$$

where X is the distance between probe tips ($X = 8$ mm herein) and T is the time for which the cross-correlation function is maximum (e.g. [16,5,15] (Fig. 4). In highly aerated free-surface flows, the validity of Eq. (1) was verified

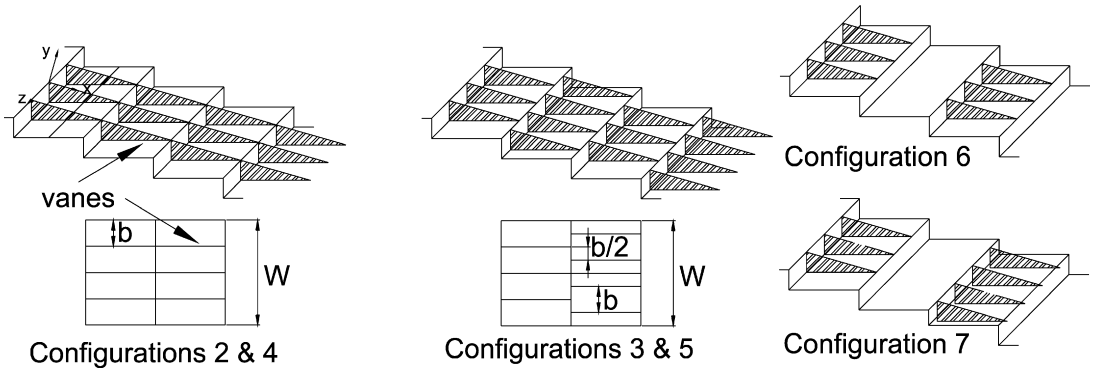

(A)

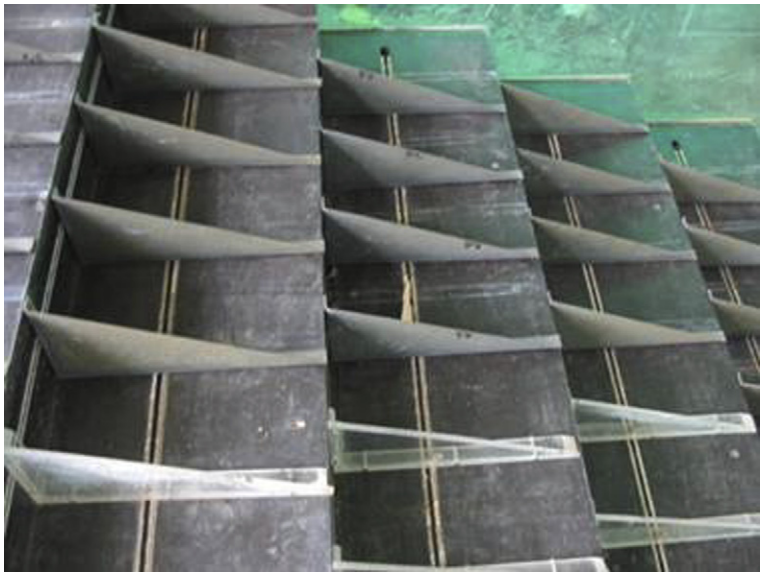

(B)

Fig. 3. Stepped chute with the different vane configurations. (A) Sketch of the configurations. (B) Photograph of the configuration 5 with seven vanes per step placed in zigzag.

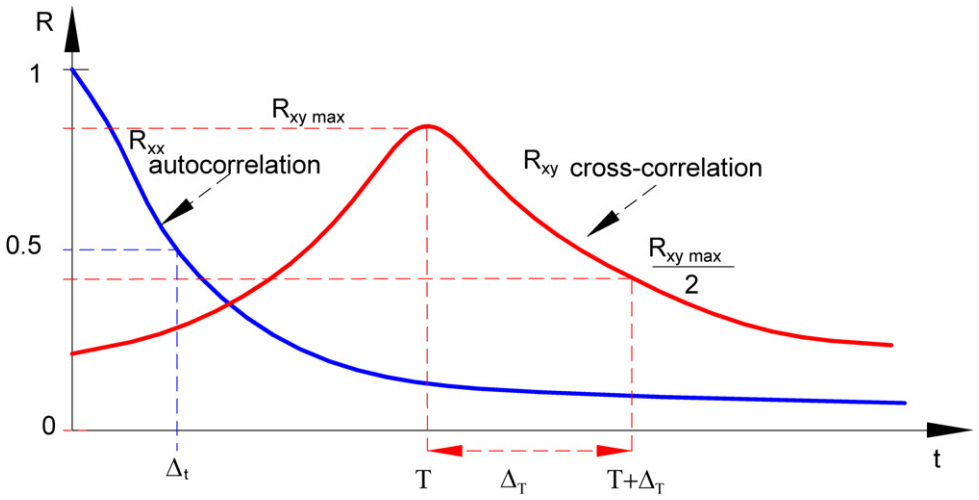

Fig. 4. Sketch of the auto- and cross-correlation functions for a dual-tip probe.

by comparisons with video observations of droplet velocity in the spray region. It was also checked successfully with the measured water fluxes deduced from measured void fraction and interfacial velocity distributions:

$$q_w = \int_{y=0}^{Y_{90}} (1 - C) \times V \times \mathrm{d}y \tag{2}$$

where q_w is the water discharge per unit width, y is the distance normal to the invert and Y_{90} is the distance where $C = 0.9$ (90%). The turbulence intensity Tu may be derived from the comparison between the broadening of the cross-correlation and auto-correlation functions:

$$Tu = 0.851 \times \sqrt{\frac{\Delta T^2 - \Delta t^2}{T^2}} \tag{3}$$

where ΔT is a time scale satisfying: $R_{xy}(T + \Delta T) = 0.5 R_{xy}(T)$, Δt is the characteristic time for which R_{xx} equals 0.5, and R_{xy} and R_{xx} are the normalised cross-correlation and auto-correlation functions respectively. Eq. (3) is a measure of the average velocity fluctuations in highly turbulent bubbly flows [17]. It might not be equal to the turbulence intensity u'/V, but it provides some information on turbulence level or average velocity fluctuations. The probe signal outputs also provided a complete streamwise characterisation of the air–water flow, specifically in terms of particle chord size distribution and clustering.

2.2. Experimental accuracy

The scan rate f_{scan} tended to govern the resolution of the double-tip conductivity signal. Assuming an average bubble velocity of 3.5 m/s, with the scan frequency of 20 kHz, the smallest detectable chord length Δch was

$$\Delta ch = \frac{V}{f_{\text{scan}}} = 0.175 \text{ mm} \tag{4}$$

The accuracy on the interfacial velocities was similarly linked with the scanning rate. Assuming no slip between the air and water phases, the error on the time-averaged velocity measurement was

$$\frac{\Delta V}{V} = 1 - \frac{1}{1 + \frac{V}{f_{\text{scan}} \times X}} = 2.2\% \tag{5}$$

where X is the longitudinal distance between probe sensors. The results (Eqs. (4) and (5)) show that the scan rate, and not the sensor diameter ($\varnothing = 0.025$ mm), limited the data accuracy.

The error on the void fraction was estimated as $\Delta C < 2\%$ using strobe light photographs of hypodermically controlled injected bubbles striking the probe-tip at the top of a water column [18,19]. The error on the bubble frequency measurements depended upon the characteristic bubble sizes, probe electrode size, scanning rate and flow velocity. For the double-tip conductivity it was estimated as $\Delta F/F < 0.5\%$ by comparing the bubble chord size distribution with the total amount of detected bubbles and the minimum detectable chord length size [17].

The error in the longitudinal translation of the probe was estimated as $\Delta x < 5$ mm. In the transverse position the error was estimated as $\Delta z < 5$ mm. The error on the probe location in the direction normal to the flow was $\Delta y < 0.025$ mm.

2.3. Measurement locations

For each configuration, the air–water flow measurements were repeated systematically at each step edge downstream of the point of inception of aeration, at several longitudinal positions in between adjacent step edges, and at several transverse positions for several flow rates.

For configuration 1 (without vanes), measurements were conducted with the double-tip probe located at the channel centreline. In the y-direction normal to the flow, measurements were taken from $y = 0$ (i.e. pseudo-bottom formed by step edges) up to the spray region. In the longitudinal direction, measurements were performed at each step edge and in between consecutive step edges at dimensionless distances $X_0 = 0.25$, 0.5 and 0.75 where $X_0 = x/L_{\text{cav}}$, x is the distance from the upper step edge to the probe-tip and L_{cav} is the distance between adjacent step edges (Fig. 3A).

For configurations 2 to 7 (with vanes), measurements were additionally carried out at three dimensionless transverse positions $z/b = 0$, 0.25 and 0.5 along the chute width, where z is the transverse direction of the chute and b is the spacing between vanes. Herein $z/b = 0$, coincides with the channel centreline above a series of vanes in configurations 2, 4 and 6 (Fig. 3). In the directions parallel and normal to the flow, measurements were performed as for configuration 1. Such a systematic experimental data set provided precise information to investigate the effects of vanes interfering on the highly turbulent aerated flows flowing down a stepped chute.

More than 240 vertical profiles were recorded with a minimum of 25 measurement points per profile. Further details on the experiments were reported in [20].

3. Basic air–water flow properties

3.1. Flow patterns

In skimming flows, the water free-surface was smooth and no air entrainment occurred at the upstream end of the chute (Fig. 5A). Next to the upstream inlet, a bottom boundary layer developed. After a few steps, the outer edge of the boundary layer reached the water free surface inducing natural flow aeration and giving the flow a white, foamy appearance (Fig. 5B). At the inception of free-surface aeration, the flow was rapidly varied (Fig. 5B). Side view observations suggested that some air was entrapped by a flapping mechanism in the step cavity(ies) immediately upstream of the visual location of free-surface aeration. Downstream of the point of inception of air entrainment, the flow behaved as an air–water homogeneous mixture and the exact location of the interface became undetermined. Intense recirculation vortices were observed between the step edges beneath the mainstream. There were continuous exchanges of air and water and of momentum between main stream and atmosphere (Fig. 5C). In the direction normal to the flow, the mainstream air–water flow consisted of three zones: a bubbly flow region ($C < 0.3$), a spray region ($C > 0.7$) and an intermediate flow zone for $0.3 < C < 0.7$, where C is the void fraction or air concentration.

Flow visualisations next to the chute sidewall and near the inception point of free-surface aeration highlighted some effect of vanes on the cavity recirculation. In presence of vanes, some cavity aeration was observed two to three step cavities upstream of the point of inception, while only one to two aerated cavities were observed in absence of vanes. Although the vanes did not interfere with the stream flow, they were subjected to strong transverse pressure forces. The pressure load fluctuations appeared to be of similar period and were in phase with observed cavity fluid ejections described by Djenidi et al. [7] for d-type roughness flow and by Chanson et al. [21] for stepped chute flows.

In configurations with vanes in-line (config. 2, 4 and 6), visual observations tended to suggest the development of a longitudinal trough above each vane.

3.2. Void fraction and bubble count rate distributions

Detailed measurements of void fraction were conducted downstream of the point of inception of air entrainment at and in between step edges. For all channel configurations, the void fractions distributions at the step edges showed some smooth S-shaped profiles that followed closely an analytical solution of the bubbles advective diffusion equation:

$$C = 1 - \tanh^2\left(K' - \frac{\frac{y}{Y_{90}}}{2 \times D'} + \frac{(\frac{y}{Y_{90}} - \frac{1}{3})^3}{3 \times D'}\right) \quad (6)$$

where Y_{90} is the distance normal to the flow for $C = 0.90$, K' and D' are integration constants functions of the mean void fraction only [17]. Between step edges, a strong aeration was recorded in the step cavities ($y < 0$). Overall, the present results showed little effect of the vanes on the void fraction data, but immediately above the vanes ($z/b = 0$, config. 2 and 4 and 6). Typical results are presented in Fig. 6 where the void fraction data are compared with Eq. (6). The data were obtained at the same identical location for one flow rate ($d_c/h = 1.5$, $Re = 7.3\,\mathrm{E} + 5$) where d_c is the critical flow depth, h is the vertical step height and Re is the flow Reynolds number. Fig. 6A presents the results obtained at step edge 9. Fig. 6B shows the data measured above the cavity between step edges 9 and 10 at the location $X_0 = 0.25$ where $X_0 = x/L_{cav}$. For this flow rate ($d_c/h = 1.5$), the inception point of free-surface aeration was located at step edge 7, and the flow at steps 9 and 10 was gradually-varied.

The bubble count rate distributions obtained at all measurement locations showed a shape with a marked maximum in the intermediate region between bubbly flow and spray regions (i.e. $0.3 < C < 0.7$). This is seen in Fig. 7 for some

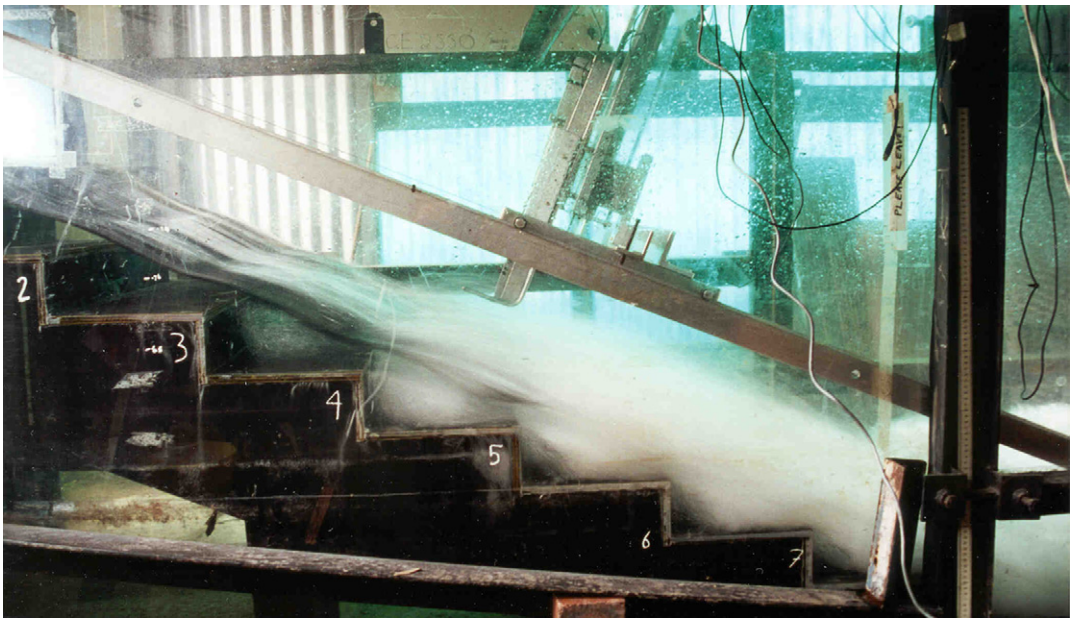

(A)

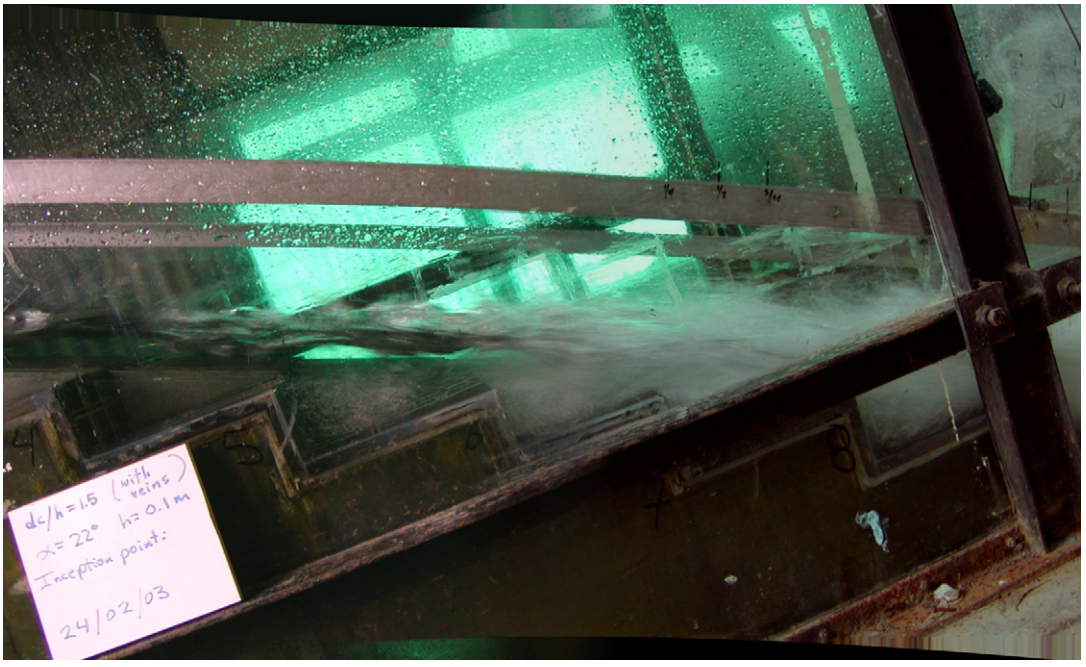

(B)

Fig. 5. Photographs of skimming flow down the stepped channel. (A) Configuration 1, $d_c/h = 1.1$, $Re = 4.4\,\mathrm{E} + 5$. (B) Skimming flow conditions next to the inception point of free-surface aeration (configuration 3, $d_c/h = 1.5$, $Re = 7.3\,\mathrm{E} + 5$) – flow from left to right. (C) Spray and droplet generation captured with high shutter speed, looking downstream (configuration 2, $d_c/h = 1.1$, $Re = 4.4\,\mathrm{E} + 5$) – note the large water projection in front of the trolley system on the right (D).

data at a step edge (Fig. 7A) and above a cavity (Fig. 7B). The data were similar for all configurations although some slightly higher bubble count rates tended to be observed immediately above the vanes ($z/b = 0$). The dimensionless bubble count rate ($F/F_{\max}$) is shown as function of the void fraction in Fig. 8, where $F_{\max}$ is the maximum bubble count rate in the cross-section. The relationship between bubble count rate and void fraction showed consistently a

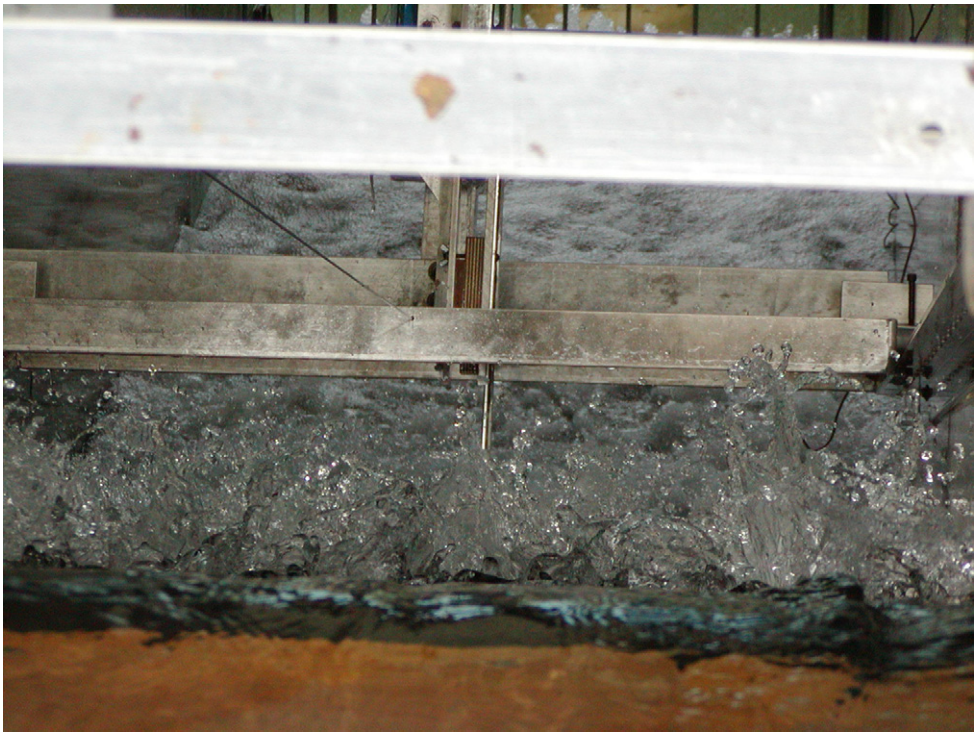

(C)

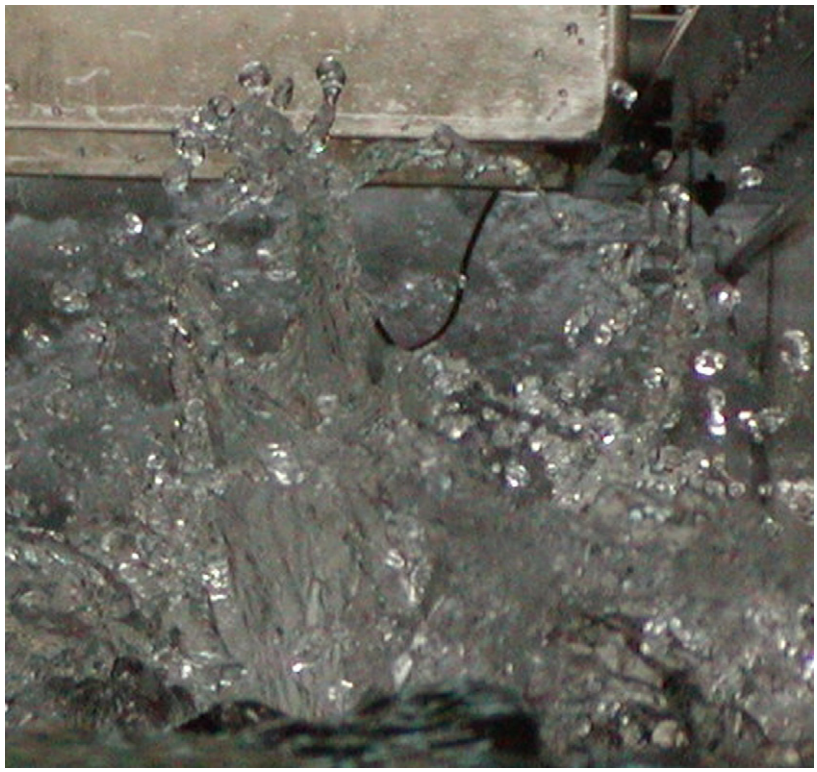

(D)

Fig. 5. (*continued*)

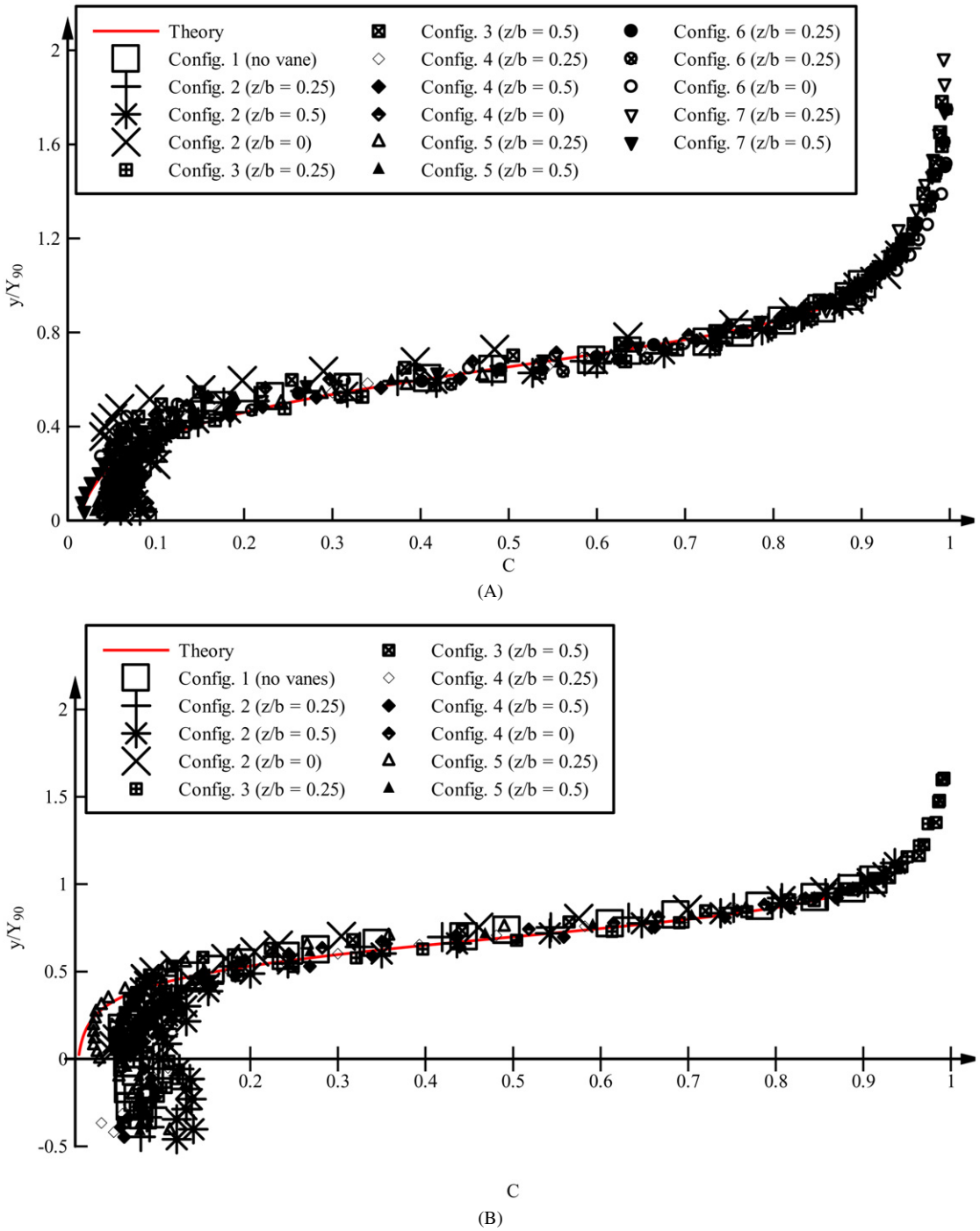

Fig. 6. Dimensionless distributions of void fraction – comparison with Eq. (6). (A) $d_c/h = 1.5$, $Re = 7.3\,\mathrm{E} + 5$, step edge 9 – all configurations. (B) $d_c/h = 1.5$, $Re = 7.3\,\mathrm{E} + 5$, above the cavity between step edges 9 and 10 ($X_0 = 0.25$) – configurations 1 to 5.

quasi-parabolic shape. Previous studies observed that the relationship between air concentration and bubble count rate followed such a parabola for a number of turbulent flow situations, including free-surface aeration in open channel flows, two-dimensional free-falling jets and turbulent shear region of hydraulic jumps [22,23]. These data were fitted

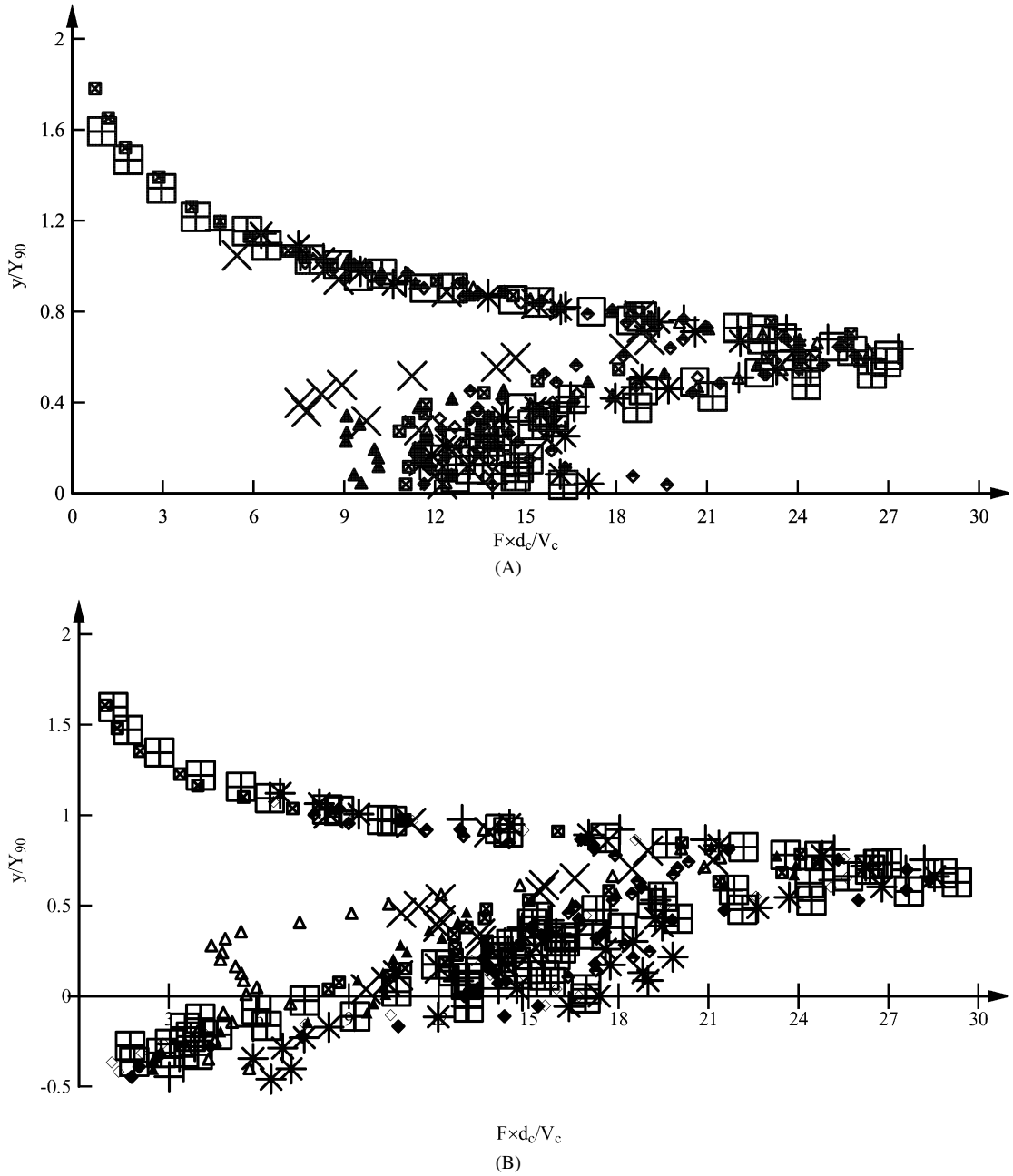

Fig. 7. Dimensionless distributions of bubble count rate (same legend as Fig. 6). (A) $d_c/h = 1.5$, $Re = 7.3\,\mathrm{E} + 5$, step edge 9 – configurations 1 to 5. (B) $d_c/h = 1.5$, $Re = 7.3\,\mathrm{E} + 5$, above the cavity between step edges 9 and 10 ($X_0 = 0.25$) – configurations 1 to 5.

by

$$\frac{F}{F_{\max}} = 4 \times C \times (1 - C) \tag{7}$$

Toombes [14] developed a modified parabolic model that best correlated stepped chute flows experimental data

$$\frac{F}{F_{\max}} = \frac{1}{\alpha(C) \times \beta(C)} \times \frac{C \times (1 - C)}{C_{\mathrm{Fmax}}^2} \tag{8}$$

where $\alpha(C)$ and $\beta(C)$ are correction factors, and C_{Fmax} is the void fraction corresponding to the maximum bubble count rate $F_{\max}$ [14]. A comparison between present experimental data and Eqs. (7) and (8) is presented in Fig. 8.

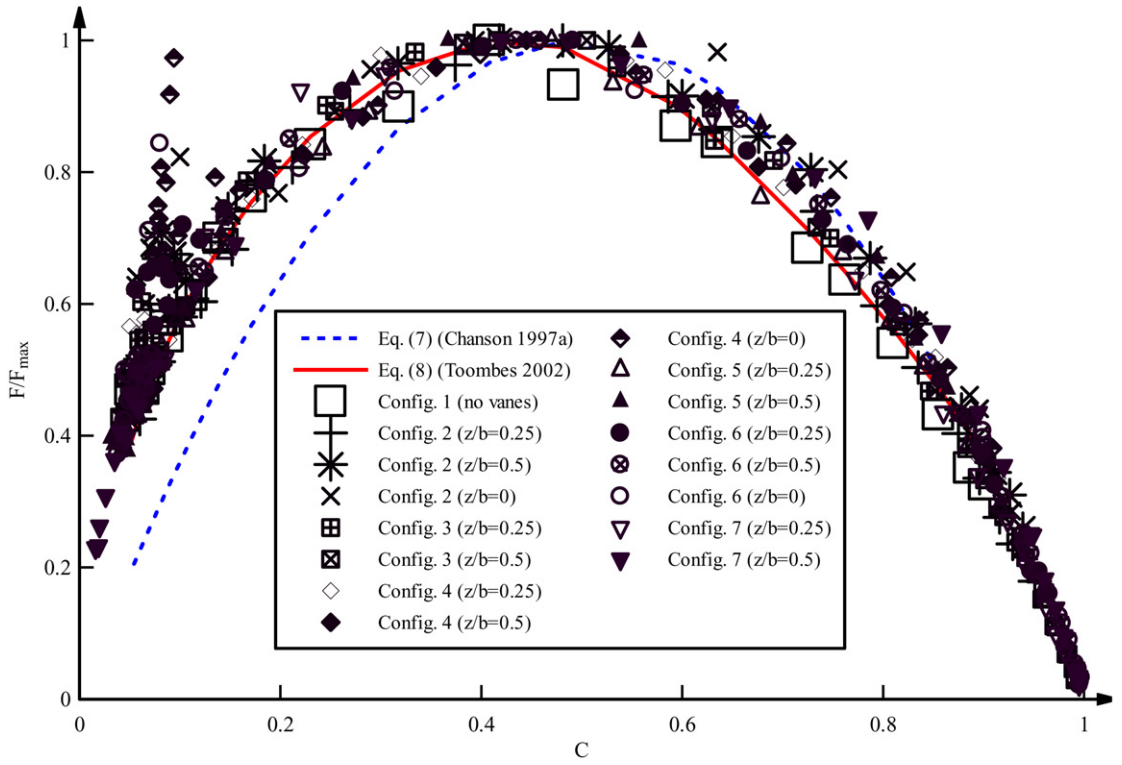

Fig. 8. Dimensionless relationship between void fraction and bubble count rate: $d_c/h = 1.5$, $Re = 7.3\,\mathrm{E} + 5$, step edge 9, all configurations – comparison with Eqs. (7) and (8).

Although the parabolic curve (Eq. (7)) fitted the data, Eq. (8) correlated best with the present experiments for all configurations.

3.3. Velocity and turbulence intensity distributions

The interfacial velocity data showed some effects of the vanes on the flow properties. This is illustrated in Fig. 9 which presents some dimensionless velocity data at a step edge. The data obtained with the reference configuration (config. 1, no vane) are highlighted with empty squares. At step edges, these data compared successfully with a power law for $y/Y_{90} < 1$ and the velocity distribution was quasi-uniform above:

$$\frac{V}{V_{90}} = \left(\frac{y}{Y_{90}}\right)^{1/N} \qquad 1 < \frac{y}{Y_{90}} \tag{9a}$$

$$\frac{V}{V_{90}} = 1 \qquad \frac{y}{Y_{90}} > 1 \tag{9b}$$

where V_{90} is the characteristic velocity at $y = Y_{90}$. Eq. (9) is shown in Fig. 9 assuming $N = 7$. The present data showed however that the effect of the vanes was not limited to the cavity flow but extended into the main stream. For configurations with vanes, the velocity distributions showed some marked differences at all transverse locations, specifically for $y/Y_{90} < 0.6$ to 0.7 (Fig. 9). The velocity measurements between step edges indicated further a developing mixing layer downstream of each step edge. This was best observed for $-0.3 < y/Y_{90} < 0.2$ [24]. The velocity observations showed some low-velocity region for $y/Y_{90} < 0.5$ above the vanes ($z/b = 0$).

In skimming flows, the distributions of turbulence intensity indicated high turbulence levels for all configurations especially in the intermediate zone ($0.3 < C < 0.7$) (Fig. 10). This trend differed from well-known turbulence intensity profiles observed in the outer region of turbulent boundary layers above smooth and rough walls. Turbulence values measured between step edges showed values approximately 40% larger for configurations with vanes than

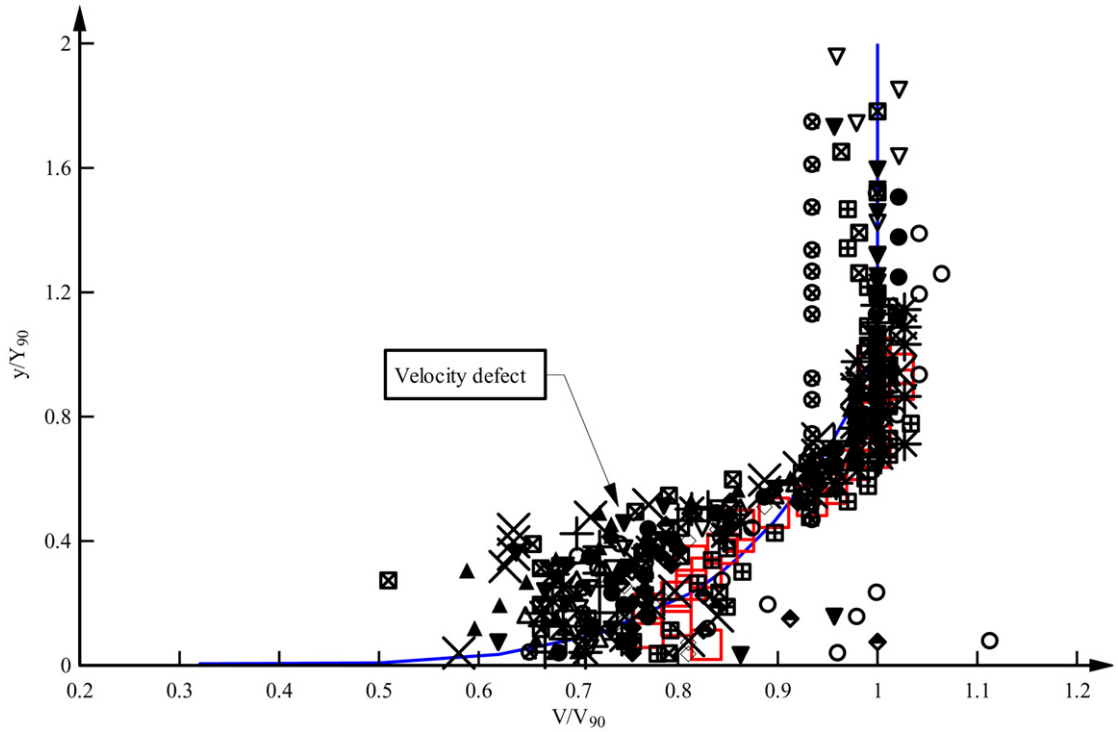

Fig. 9. Dimensionless distributions of interfacial velocity for $d_c/h = 1.5$, $Re = 7.3\,\mathrm{E}+5$, step edge 9, all configurations (same legend as Fig. 6) – comparison with Eq. (9).

those for configuration 1 (no vanes) (Fig. 10B). The maximum turbulence levels were observed for the configurations with vanes in zigzag, suggesting that the distribution of the vanes has a larger effect than the number of vanes placed across the chute width.

It is proposed that the large turbulence levels were linked to the number of entrained bubbles/droplets within the flow. This is illustrated in Fig. 11 presenting the dimensionless relationship between turbulence intensity and bubble count rate. Figs. 11A and 11B show some data obtained at step edges and in between step edges respectively. In a cross-section, the turbulence intensity was correlated with the bubble count rate by

$$Tu = 0.25 + k \times \left(\frac{F \times d_c}{V_c}\right)^{1.5} \tag{10}$$

where k is a constant which is a function of the step geometry, location and flow rate. Eq. (10) is compared with experimental data in Fig. 11. It reflects an increase in turbulence associated with the number of entrained particles. It is believed that the large number of gas–liquid interfaces, and the continuous deformations of the air–water structures caused these large turbulence levels.

3.3.1. Discussion

During the early stages of the study, it was expected that the ribs would affect primarily the cavity flow. Yet the experimental evidence showed that the effects of the ribs extended beyond the cavity regions and affected some air–water flow properties in the free-stream region including the velocity and turbulence level profiles (Figs. 9 and 10). We hypothesise that the presence of the ribs affected primarily the microscopic flow structures rather than the rate of entrained air, hence the void fraction distributions. Indeed the free-surface aeration is primarily a function of the turbulence acting next to the free-surface which was relatively little affected by the ribs.

It is proposed that the effects of the vanes onto the main flow were three-fold. First the presence of vanes prevented the spanwise development of large coherent vortical structures in the step cavities ($y < 0$). Second, they enhanced the spray production. Third the vanes led to the appearance of longitudinal (streamwise) troughs in the mainstream flow

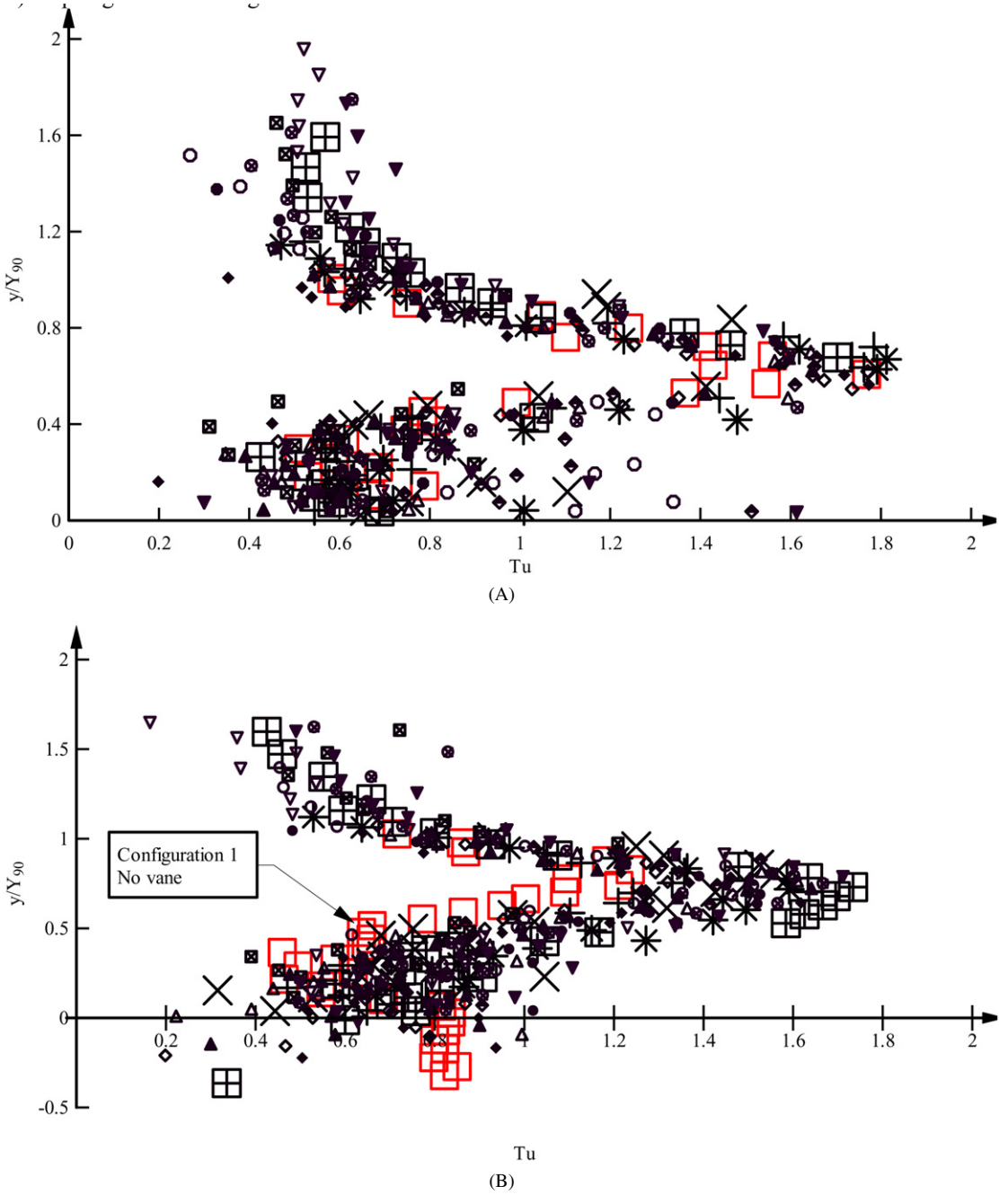

Fig. 10. Dimensionless distributions of turbulence intensity for $d_c/h = 1.5$, $Re = 7.3\,\mathrm{E}+5$ (same legend as Fig. 6). (A) Step edge 9 – all configurations. (B) Above the cavity between step edges 9 and 10 ($X_0 = 0.25$) – all configurations.

($y > 0$). Such coherent structures affected momentum exchange between cavity and stream flows and hence the rate of energy dissipation.

The presence of vanes prevented the transverse development of large-scale turbulence in the cavities. The inhibition of large transverse vortical structures was associated with enhanced vertical mixing between recirculation zones and mainstream that was characterised by irregular fluid ejections, turbulent bursts and sweeps. It is suggested that some modification of the mixing layer developing downstream of each step edge was associated with greater rates of

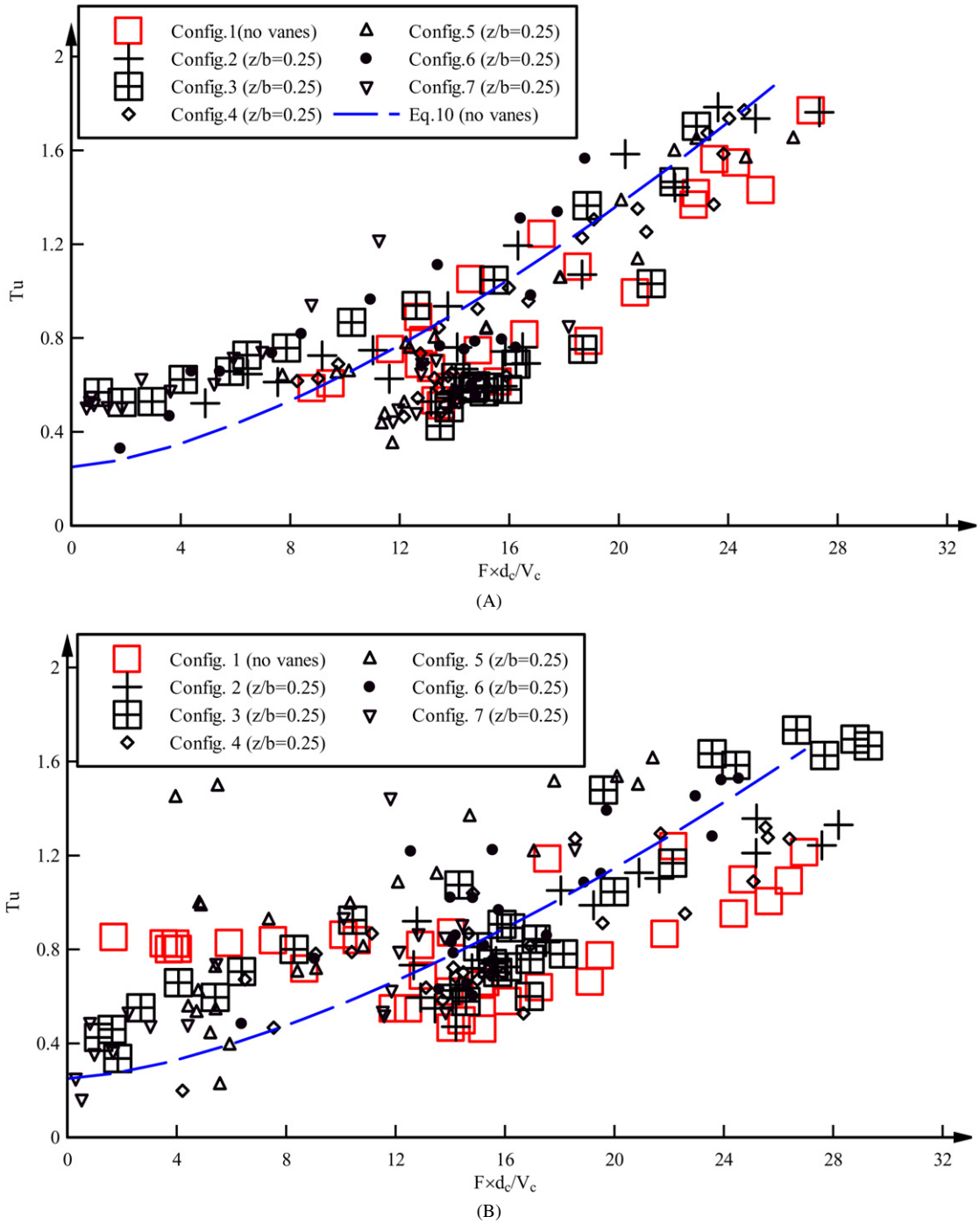

Fig. 11. Dimensionless relationship between bubble count rate and turbulence intensity for $d_c/h = 1.5$, $Re = 7.3\,\mathrm{E}+5$ – comparison with Eq. (10). (A) Step edge 9. (B) Above the cavity between step edges 9 and 10 ($X_0 = 0.25$).

expansion and larger transfer of momentum from free-stream to cavity flow (Fig. 12). Turbulent mixing enhancement was further associated with the development of streamwise coherent vortices in the main stream.

The large vertical mixing was associated with a stronger spray generation above the free-surface, for the configurations with vanes. If the water volume flux in the "mist" region is defined as:

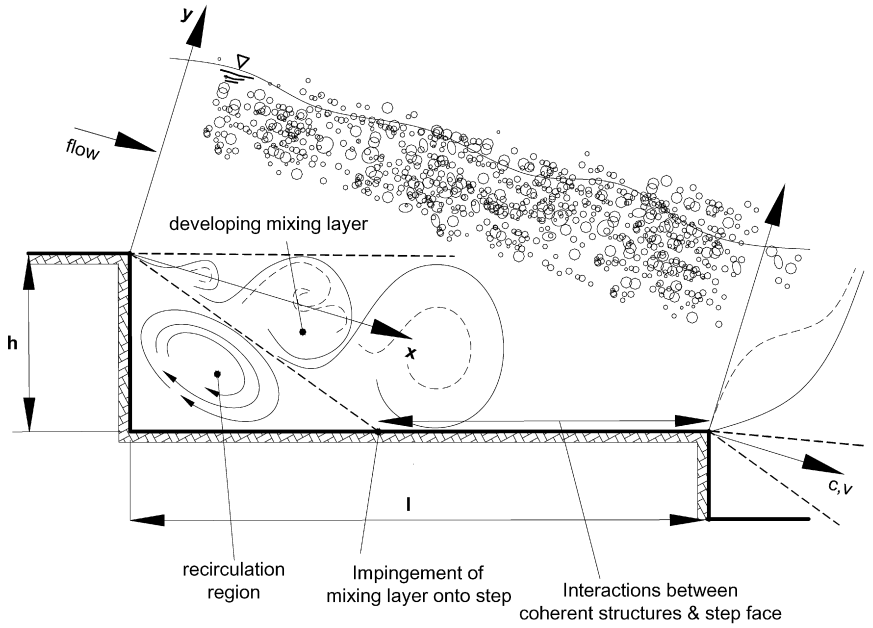

Fig. 12. Sketch of the mixing layer development downstream of each step edge and of the re-attachment on the horizontal step face.

$$q_{\text{mist}} = \int_{y=Y_{90}}^{Y_{99}} (1-C) \times V \times \mathrm{d}y \tag{11}$$

with Y_{99} the distance where $C = 0.99$, the experimental data showed consistently that the dimensionless water flux in the mist q_{mist}/q_w was about 5–10% in absence of vane (config. 1) and increased to about 20–30% for configurations with vanes. The largest mist flux was observed for configuration 2 although there was little difference among the rest of them.

Visual observations suggested the existence of longitudinal troughs above the vanes ($z/b = 0$), while the velocity data suggested some low-velocity region for $y/Y_{90} < 0.6$ (Fig. 8). These findings may suggest the existence of longitudinal vortical structures above the vanes. Holmes et al. [25] proposed the existence of pairs of counter-rotating streamwise vortices or "rolls" next to the wall in turbulent boundary layers, associated with a region of reduced velocity in the stream direction. Herein, the longitudinal troughs above the vanes were somehow similar to low-speed streaks interfering with the main stream. Such turbulent structures were best observed next to the inception point of free-surface aeration, but they were believed to occur further downstream.

4. Air–water flow structures

4.1. Air and water chord length distributions

In highly-turbulent open channel flows, the air bubble entrainment is uncontrolled and the air–water flow mixture contains a broad range of air bubble and water droplet sizes. With an intrusive phase-detection probe, the flow may be analysed in terms of the streamwise air and water chords bounded by air–water interfaces. In bubbly flows with low void fractions ($C < 0.10$), the chord measurements may be transformed into some characteristic bubble diameter/size distribution with a minimum number of assumptions on the bubble shape (e.g. [26,27]). Such a technique is not appropriate for large void fractions because the shapes of the air–water structures are unknown. The data are instead presented in the form of probability distribution functions (PDF) of chord sizes. Figs. 13 and 14 present some typical PDFs of bubble and droplet sizes for the present data. These data were recorded at the same cross-section and for the same flow conditions as the data shown in Figs. 6 to 10. In a histogram, each column represents the probability of air/water structures with chords within a 0.5 mm range: e.g. the column with 1 mm represents the probability of

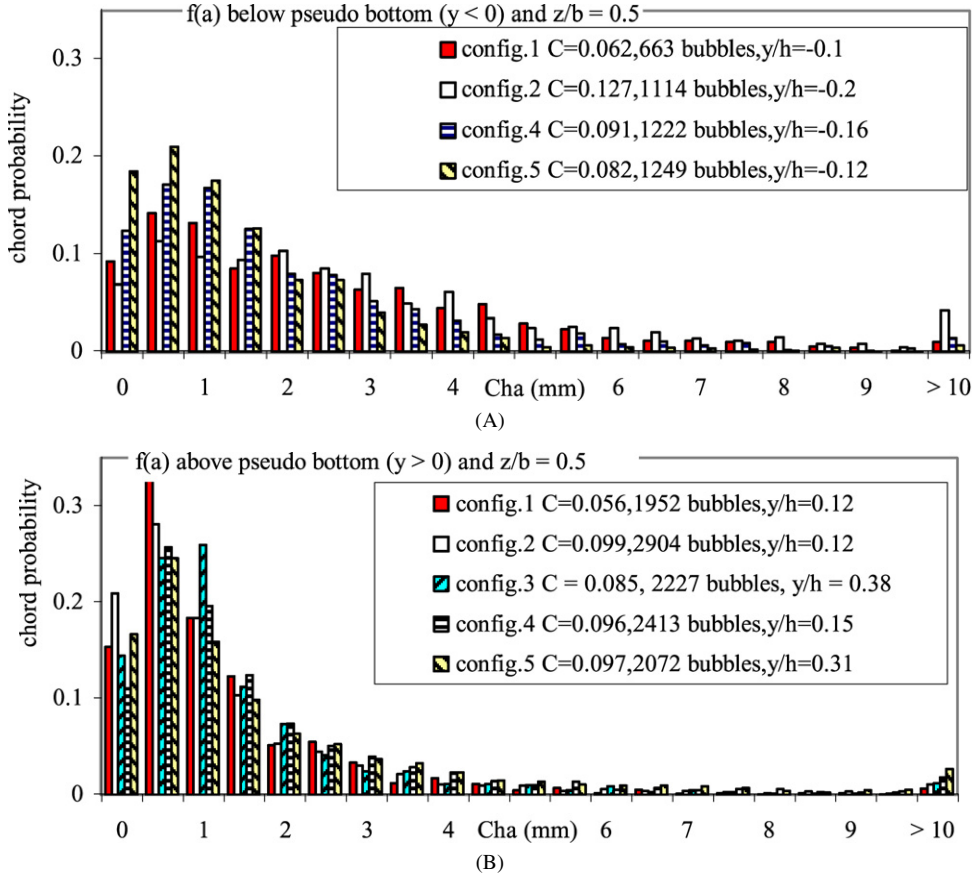

Fig. 13. Probability distribution functions of air bubble chord sizes in the bubbly flow region ($C < 0.3$) for $d_c/h = 1.35$, $Re = 6.5\,\mathrm{E} + 5$, between step edges 9 and 10 ($X_0 = 0.25$), $z/b = 0.5$. (A) Bubble chord sizes in the step cavity ($y < 0$) for configurations 1 to 5. (B) Bubble chord sizes above the step cavity ($y > 0$) for configurations 1 to 5.

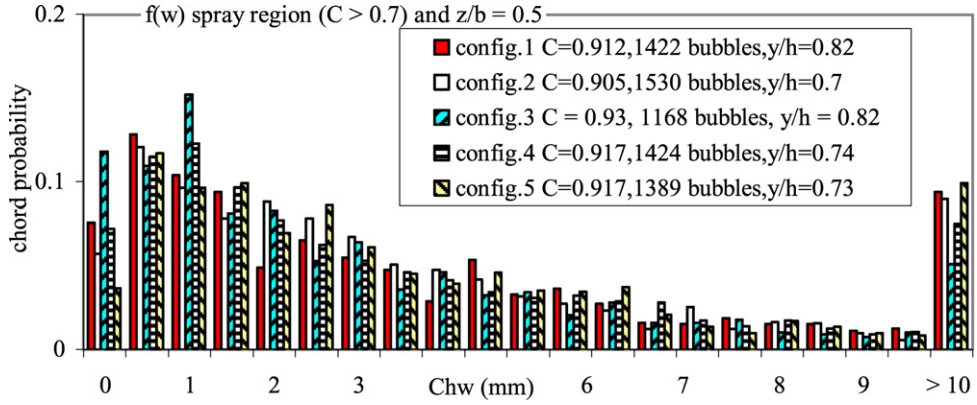

Fig. 14. Probability distribution functions of water droplet chord sizes in the spray region ($C > 0.7$) for $d_c/h = 1.35$, $Re = 6.5\,\mathrm{E} + 5$, between step edges 9 and 10 ($X_0 = 0.25$), $z/b = 0.5$, configurations 1 to 5.

chords between 1 and 1.5 mm. Further the figure caption and legend give some details on the local air–water flow properties including the void fraction and bubble number.

For all configurations, the PDFs of bubble chords were skewed with a preponderance of chord sizes smaller than the mean. Fig. 13A presents typical bubble chord PDFs measured in between vanes ($z/b = 0.5$) below the pseudo-bottom

($y < 0$). The reference geometry data (config. 1, no vane) are shown in dark red.[2] Fig. 13B shows some bubble chord data measured above the pseudo-bottom ($y > 0$) in similar conditions and with similar air concentrations as in Fig. 13A. The mode was typically between 0.5 and 1.5 mm although a broad range of chord sizes was detected (Fig. 13). In the main stream ($y > 0$), the experimental results showed consistently a large number of detected bubbles than the amount of bubbles detected in the cavity recirculation region ($y < 0$) for similar void fractions ($C \sim 0.1$). Although the histogram mode was 0.5–1.5 mm for both locations (i.e. $y < 0$ & $y > 0$), the bubble chord distributions in the step cavity ($y < 0$, Fig. 13A) were flatter than those within the mainstream (Fig. 13B) implying the existence of larger bubbles in the recirculation region.

Fig. 14 shows typical PDFs of droplet sizes in the spray region ($C > 0.7$) for the same flow conditions and at the same cross-sections as the data shown in Fig. 13. The predominant water chords were between 0.5 and 2 mm. However a wide range of droplet sizes was observed: e.g., 75% of the water droplets had sizes varying from 1 to 8.5 mm.

4.1.1. Remarks

The present results tended to show that the bubble/droplet size distributions were affected by the presence of vanes. This was mainly observed in the bubbly flow region of the mainstream ($y > 0$, $C < 0.3$) where a broadening of bubble chord PDFs was observed in presence of vanes (Fig. 13B). The bubble size distribution functions were less skewed and peaky in presences of vanes. Further a greater spray production and droplet numbers were observed in the upper spray region for the configurations with vanes.

4.2. Clustering analysis

The existence of particle clusters may be related to break-up, coalescence and other processes. In turbulent flows, air bubbles may be trapped in coherent structures. In a cluster, the particles are close together and the group (convoy) is surrounded by a sizeable volume of the other phase. In the present study, bubble and droplet grouping analyses were performed in the streamwise direction only. A clustering analysis was developed based upon a few assumptions. A cluster was defined as two or more particles (bubbles/droplets) were grouped together one after another, travelled with the same velocity and distinctly separated from other particles before and after the cluster/packet. In bubbly flow ($C < 0.3$) two bubbles were considered to form a cluster when they were separated by a water chord length (ch_w) smaller than one tenth of the mean water chord size ($ch_w < 0.1 \times \overline{ch_a}$) [17]. In the spray region ($C > 0.7$), two droplets were assumed to cluster when they were separated by an air chord (ch_a) smaller than one tenth of the mean air chord size ($ch_a < 0.1 \times \overline{ch_w}$).

At locations in the step cavities ($y < 0$), about 15% of all bubbles were "clustered" in the streamwise direction. Measurements above the pseudo-bottom ($y > 0$) showed nearly identical results in the bubbly flow region ($C < 0.3$). In the mist region ($C > 0.9$), however, only 5% of water droplets were clustered. Interestingly the results were nearly identical for all seven step arrangements. Further the distributions of particle number per cluster were analysed. Typical results are shown in Figs. 15 and 16, for the bubbly flow and spray regions respectively. Overall, the cluster analysis results showed a fair proportion of bubbles travelling as part of a cluster, and most clusters were made of two-particle structures. The findings were in agreement with previous observations by Chanson and Toombes [17]. Note however that their analysis, as well as the present study, were restricted to longitudinal flow direction and did not consider particles travelling side by side.

4.2.1. Discussion

Downstream of each step edge, a shear layer developed where eddies grew by a pairing process while they are advected (Fig. 12). Once the coherent structures reached a size comparable to the step cavity height, the vortices interacted with the horizontal step face and interact with the solid boundaries. Visual observations showed that some cavity fluid ejection took place, at irregular time intervals, primarily at the downstream end of the cavity. Despite some basic difference between the upstream (undisturbed) and downstream shear zones, present results showed that the flow structure (chord size distributions, particle grouping) did not vary much with the streamwise position X_0 along the cavity length. It was further unaffected by the flow Reynolds number within the range of the investigations.

[2] For colours see the web version of this article.

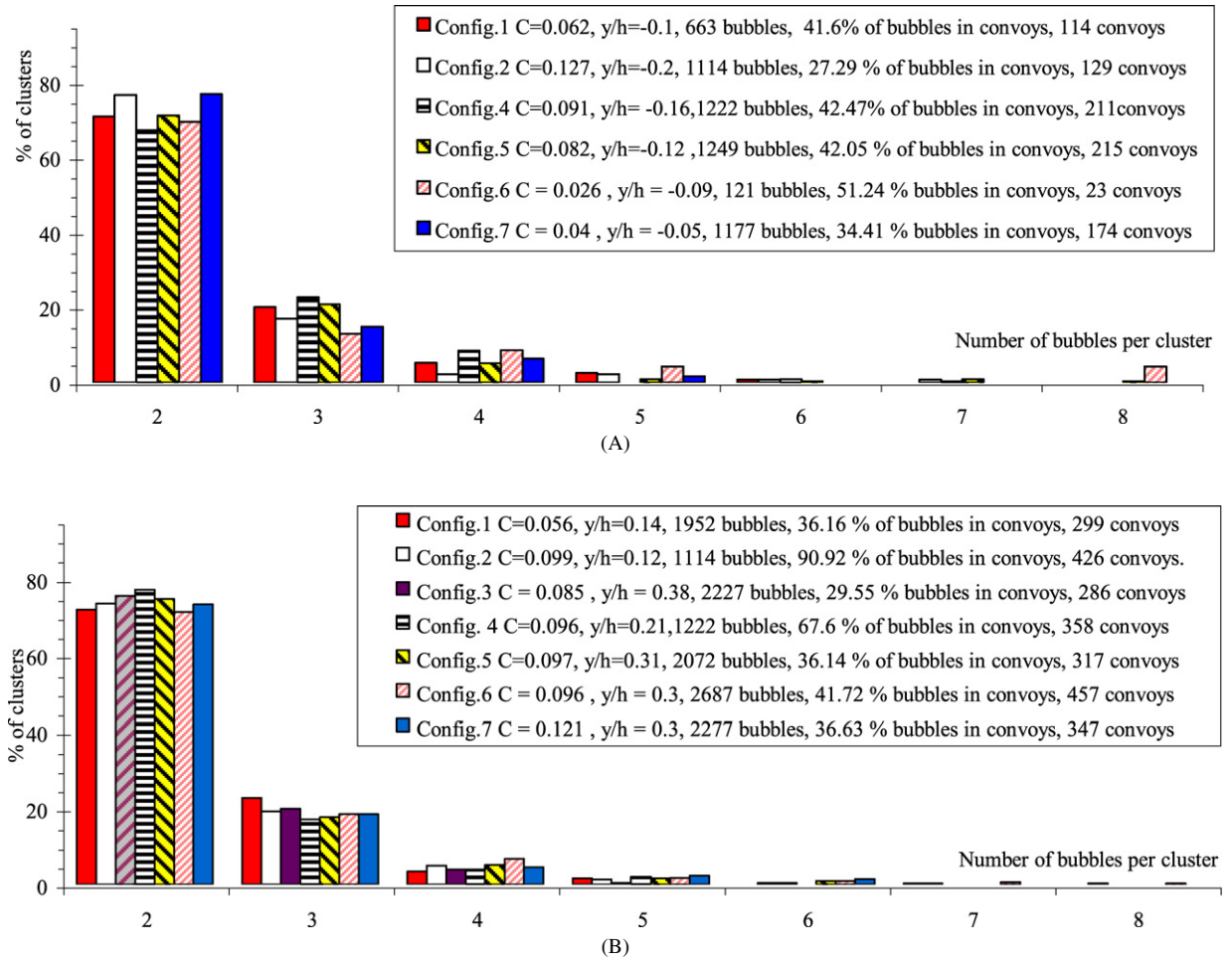

Fig. 15. Number of bubbles per cluster in the bubbly flow region ($C < 0.3$) for $d_c/h = 1.35$, $Re = 6.5\,\mathrm{E} + 5$, between step edges 9 and 10 ($X_0 = 0.25$), $z/b = 0.5$. (A) Clustering in the step cavity ($y < 0$). (B) Clustering above the step cavity ($y > 0$).

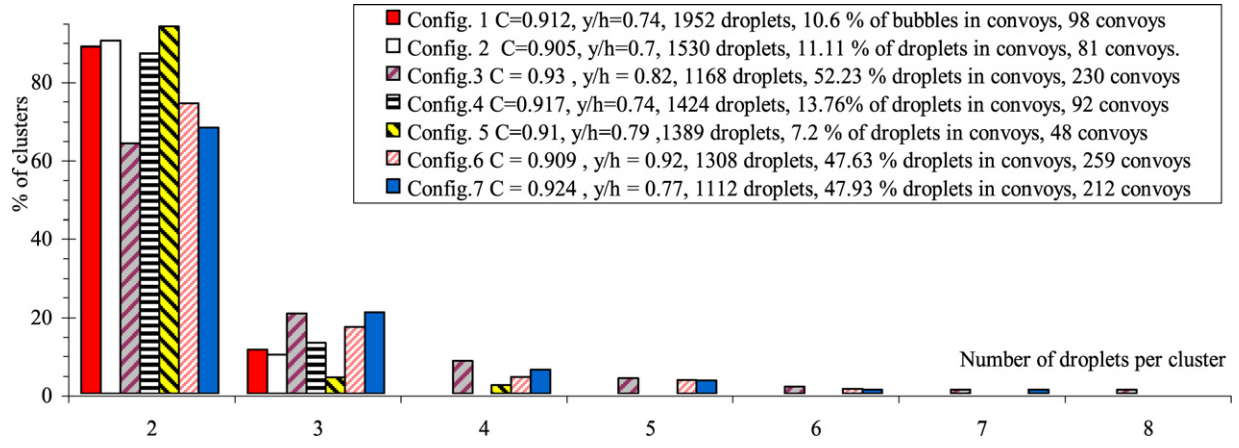

Fig. 16. Number of bubbles per cluster in the mist region ($C < 0.9$) for $d_c/h = 1.35$, $Re = 6.5\,\mathrm{E} + 5$, between step edges 9 and 10 ($X_0 = 0.25$), $z/b = 0.5$.

5. Conclusion

The interactions between free-surface aeration, turbulence and cavity recirculation were investigated in skimming flows down a stepped channel in a large-size facility operating at large Reynolds numbers. Passive turbulence manipulation was systematically tested. Seven stepped geometries were studied. For six configurations, some turbulence manipulators were introduced in the form of triangular vanes, or longitudinal ribs, placed across the step cavity to block the development of three-dimensional recirculation without intruding into the free-stream.

The basic results showed that the vanes had little effect on the distributions of void fraction and bubble count rate distributions, except immediately above the vanes. But the results showed that the vanes had some influence on the distributions of interfacial velocity and turbulence intensity in both free-stream and cavity flows. The presence of vanes had several effects on the flow field. The longitudinal ribs prevented the spanwise development of large recirculating eddies in the step cavities, and enhanced the spray and mist production, while they contributed to the development of longitudinal troughs above each vane. Further, the air–water chord size distributions were affected by the presence of vanes, particularly in the bubbly flow region of the mainstream.

The present results tended to suggest that the configurations with vanes in zigzag (config. 3 and 5) had a greater impact on the air–water flow properties, while the results with vanes placed every two steps (config. 6 and 7) showed little difference with the reference geometry (config. 1, no vane). Overall the study provided new information on the complex interactions between turbulence and flow aeration in open channel flows with large Reynolds numbers. The results demonstrated some successful passive turbulence manipulation in high-velocity free-surface flows.

Acknowledgements

The writers thank Mr G. Illidge for his technical assistance and Professor C.J. Apelt for his valuable advice. The first writer acknowledges the financial support of the National Council for Science and Technology of Mexico (CONACYT) and of the University of Queensland.

References

[1] O.C. Jones, J.M. Delhaye, Transient and statistical measurement techniques for two-phase flows: A critical review, Int. J. Multiphase Flow 3 (1976) 89–116.
[2] W.D. Bachalo, Experimental methods in multiphase flows, Intl. J. Multiphase Flow 20 (Suppl.) (1994) 261–295.
[3] N.S.L. Rao, H.E. Kobus, Characteristics of Self-Aerated Free-Surface Flows, Water and Waste Water/Current Research and Practice, vol. 10, Eric Schmidt Verlag, Berlin, Germany, 1971.
[4] I.R. Wood, Air Entrainment in Free-Surface Flows, Hydraulic Design Considerations, IAHR Hydraulic Structures Design Manual, vol. 4, Balkema Publ., Rotterdam, The Netherlands, 1991, 149 pages.
[5] H. Chanson, Air Bubble Entrainment in Free-Surface Turbulent Shear Flows, Academic Press, London, UK, 1997, 401 pages.
[6] H. Chanson, The Hydraulics of Stepped Chutes and Spillways, Balkema, Lisse, The Netherlands, 2001, 418 pages.
[7] L. Djenidi, R. Elavarasan, R.A. Antonia, The turbulent boundary layer over transverse square cavities, J. Fluid Mech. 395 (1999) 271–294.
[8] O.M. Aivazian, New investigations and new method of hydraulic calculation of chutes with intensified roughness, Gidrotekhnicheskoe Stroitel'stvo 6 (1996) 27–39, (in Russian). Translated in: Hydrotechnical Construction 30 (1996) 335–356, Plenum Publ.
[9] S. Mochizuki, H. Osaka, Two-point velocity correlation measurement in a d-type rough wall boundary layer modified with the longitudinal thin ribs, in: Proc. 9th Symp. on Turbulent Shear Flows, Kyoto, Japan, Aug. 16–18, 1993, paper 5-2, 6 pages.
[10] S. Mochizuki, A. Izawa, H. Osaka, Turbulent drag reduction in a d-type rough wall boundary layer with longitudinal thin ribs placed within traverse grooves (higher-order moments and conditional sampling analysis), Trans. JSME Int. J. Ser. B 39 (3) (1996) 461–469.
[11] H. Chanson, C.A. Gonzalez, Stepped spillways for embankment dams: Review, progress and development in overflow hydraulics, in: F. Yazdandoost, J. Attari (Eds.), Proc. Intl Conf. on Hydraulics of Dams and River Structures, Tehran, Iran, Balkema Publ., The Netherlands, 2004, pp. 287–294.
[12] H. Chanson, Air bubble entrainment in free-surface turbulent flows, Experimental investigations, Report CH46/95, Dept. of Civil Engineering, University of Queensland, Australia, June, 1995, 368 pages.
[13] P.D. Cummings, Aeration due to breaking waves, Ph.D. thesis, Dept. of Civil Engrg., University of Queensland, Australia, 1996.
[14] L. Toombes, Experimental study of air–water flow properties on low-gradient stepped cascades, Ph.D. thesis, Dept of Civil Engineering, The University of Queensland, 2002.
[15] C. Crowe, M. Sommerfield, Y. Tsuji, Multiphase Flows with Droplets and Particles, CRC Press, Boca Raton, USA, 1998, 471 pages.
[16] P. Cain, I.R. Wood, Instrumentation for aerated flow on spillways, J. Hyd. Div. ASCE 107 (11) (1981) 1407–1424.
[17] H. Chanson, L. Toombes, Air–water flows down stepped chutes: Turbulence and flow structure observations, Intl. J. Multiphase Flow 28 (11) (2002) 1737–1761.

[18] P.D. Cummings, H. Chanson, Air entrainment in the developing flow region of plunging jets. Part 1: Theoretical development, J. Fluids Eng. Trans. ASME 119 (3) (1997) 597–602.
[19] P.D. Cummings, H. Chanson, Air entrainment in the developing flow region of plunging jets. Part 2: Experimental, J. Fluids Eng. Trans. ASME 119 (3) (1997) 603–608.
[20] C.A. Gonzalez, An Experimental study of free-surface aeration on embankment stepped chutes, Ph.D. thesis, Department of Civil Engineering, The University of Queensland, Brisbane, Australia, 2005, 240 pages.
[21] H. Chanson, Y. Yasuda, I. Ohtsu, Flow resistance in skimming flows and its modelling, Can. J. Civ. Eng. 29 (6) (2002) 809–819.
[22] H. Chanson, Air bubble entrainment in open channels. Flow structure and bubble size distributions, Int. J. Multiphase Flow 23 (1) (1997) 193–203.
[23] T. Brattberg, H. Chanson, L. Toombes, Experimental investigations of free-surface aeration in the developing flow of two-dimensional water jets, J. Fluids Eng. Trans. ASME 120 (4) (1998) 738–744.
[24] C.A. Gonzalez, H. Chanson, Interactions between cavity flow and main stream skimming flows: An experimental study, Can. J. Civ. Eng. 31 (1) (2004) 33–44.
[25] P. Holmes, G. Berkooz, J.L. Lumley, Turbulence: Coherent Structures, Dynamical Systems, and Symmetry, Cambridge University Press, Cambridge, UK, 1996.
[26] R.A. Herringe, M.R. Davis, Structural development of gas–liquid mixture flows, J. Fluid Mech. 73 (1976) 97–123.
[27] N.N. Clark, R. Turton, Chord length distributions related to bubble size distributions in multiphase flows, Int. J. Multiphase Flow 14 (4) (1988) 413–424.